Appl. Phys. B 71, 523–531 (2000) / Digital Object Identifier (DOI) 10.1007/s003400000361

Applied Physics B
Lasers
and Optics

Temperature distribution and thermal-induced defects in photorefractive barium titanate crystals illuminated with intense cw or pulsed laser irradiations

P. Mathey[1,*], **S. Latour**[1], **P. Lompré**[1], **P. Jullien**[1], **D. Rytz**[2], **B. Salce**[3]

[1] Laboratoire de Physique de l'Université de Bourgogne, Matériaux Photoréfractifs et Applications, Centre National de la Recherche Scientifique, Unité Mixte de Recherche 5027, 9 Avenue Alain Savary, B.P. 47870, 21078 Dijon Cedex, France
[2] Forschunginstitut für mineralische und metallische Werkstoffe, Edelsteine/Edelmetalle GmbH, Struthstrasse 2, Wackenmühle, 55743 Idar-Oberstein, Germany
[3] Centre d'Etudes Nucléaires de Grenoble, Laboratoire de Cryophysique, 38054 Grenoble Cedex 9, France

Received: 7 March 2000/Revised version: 14 April 2000/Published online: 16 August 2000 –

Abstract. The temperature distribution in a parallelepipedic crystal irradiated with a Gaussian repartition of light is calculated by solving the three-dimensional heat equation and taking into account the losses through the sides of the samples. The theoretical and experimental maps of temperature are satisfactorily compared. For barium titanate crystals, the resistance to intense cw laser (25.7 kW/mm^2 at 514.5 nm) and to Nd:YAG pulsed laser (peak power of 9.2 MW at 532 nm) is investigated. The defects induced by the irradiation are analysed. Under pulsed illumination, the damage threshold is found to be 0.54 GW/cm^2 in a nominally undoped $BaTiO_3$ and 0.44 GW/cm^2 in a rhodium-cobalt doped $BaTiO_3$ crystal.

PACS: 44.10; 42.70.Nq; 77.84.Dy

Since the development of laser rods, much attention has been devoted to the temperature distribution in these materials and to the related thermal distortions. Several studies have led to one of the most famous lasing materials: Nd:YAG. Attention has been paid to the analysis of the optical distortion induced by the pump radiation [1–3]. In the cylindrical geometry of the lasing materials, it is recognized that the heat is removed on the circumferential surface of the cylinder, thereby generating a radial thermal gradient. This change in temperature causes a thermal distortion of the laser beam due to temperature and stress variations of the refractive index [4, 5].

More recently, this problem arises in optical non-linear materials because they need strong power densities to operate. For example, this is the case in second-harmonic generation or in experiments that involve photorefractive crystals for which the response time of the phenomenon is inversely proportional to the light intensity [6–8]. In non-linear photorefractive materials, it is known that thermally induced change in index of refraction may lead to non-negligible effects [9]. In particular, in this kind of material, the influence of thermal patterns and of the induced pyroelectric fields on the photorefractive holographic recording have been calculated and it has been revealed that the pyroelectric field can enlarge the space-charge field as well as the sensitivity of holographic recording [10, 11]. Experimental studies of thermally induced self-focusing effects of light beams in photorefractive waveguides underline the role of the thermo-optic and pyroelectric effects in this class of sample [12, 13]. For each material, the relevant parameter is the damage threshold under cw or pulsed illumination. The damage threshold is defined as permanent surface damage or bulk fracture.

The aims of the present work are to analyse theoretically and experimentally the temperature distribution in crystals and to detect the defects that appear in photorefractive materials illuminated with a strong cw or a pulsed laser. The theoretical development is derived in Sect. 1. The heat conduction equation is solved at stationary state in a parallelepipedic material crossed by a beam having a Gaussian repartition of light. The heat losses at the boundaries of the crystal are taken into account. The kinetics of the temperature rise is also studied by solving the three-dimensional time-dependent heat equation. The numerical calculations are compared with the experimental results; the agreement is satisfactory. Section 2 is devoted to the experimental results. The overall optical setup useful to irradiate the crystal and to detect in real time the appearance of several kinds of defects is described. The experiments are conducted on barium titanate crystals ($BaTiO_3$) nominally undoped or doped with cobalt (Co) or rhodium (Rh). From the kinetics of the temperature when the crystal is illuminated with a cw laser beam, the time constant is deduced, this for two polarizations of the light (extrordinary and ordinary). The detection of the defects is investigated when the crystals are irradiated with an argon laser or with a pulsed Nd:YAG source.

1 Theoretical model

In this section, the temperature distribution is calculated by solving the three-dimensional steady-state heat equation. The kinetics of the temperature rise is also analysed. The heat equation is solved using the heat generated within the sample by the light beam as the source term. Most of the works

*Corresponding author. (E-mail: pmathey@u-bourgogne.fr)

published on the subject are restricted to isotropic cylindrical rods in which the heat is uniformly generated. Moreover, the fact that the laser rod may not be very long compared to its diameter is assumed so that the end effects are neglected. On these assumptions, the heat equation is written in cylindrical coordinates and gives a quadratic law for the radial steady-state temperature. Recent studies are dedicated to the heat repartition in parallelepipedic samples illuminated with pulsed lasers [14, 15]. In this regime, the adiabatic boundary conditions for the thermal flux are used. For parallelepipedic crystals having their ridges with the same order of magnitude (some millimeters), the cylindrical symmetry of the problem does not occur so that the heat equation has to be written under cartesian coordinates. Moreover the heat losses through all the faces of the material must be taken into account.

The intensity of the laser beam follows a Gaussian law and may be expressed as (the framework of the coordinate system is defined in Fig. 1) :

$$I(x, y, z) = \frac{P}{\pi w^2(z)} \mathrm{e}^{-\left[(x^2+y^2)/w^2(z)\right]} , \tag{1}$$

where P is the beam power, $w(z)$ is the half width of the beam.

In most of the non-linear optical experiments the beam is focused inside the crystal and this is the case in our studies. Since the length l_3 is smaller than the Rayleigh length of the laser beam we can set $w(z) = w_0$ where w_0 is the beam waist.

The absorption coefficient of the crystal being α, the absorbed density of power at a given point in the sample is:

$$A(x, y, z) = \frac{\alpha P}{\pi w_0^2} \mathrm{e}^{-\left[(x^2+y^2)/w_0^2\right]} \mathrm{e}^{-\alpha z} . \tag{2}$$

$A(x, y, z)$ is the source term in the heat equation if the illumination is time independent. Using cartesian coordinates, the heat equation is [16]:

$$\frac{\partial^2 T(x, y, z)}{\partial x^2} + \frac{\partial^2 T(x, y, z)}{\partial y^2} + \frac{\partial^2 T(x, y, z)}{\partial z^2} = -\frac{A(x, y, z)}{K} + \frac{1}{D}\frac{\partial T}{\partial t} , \tag{3}$$

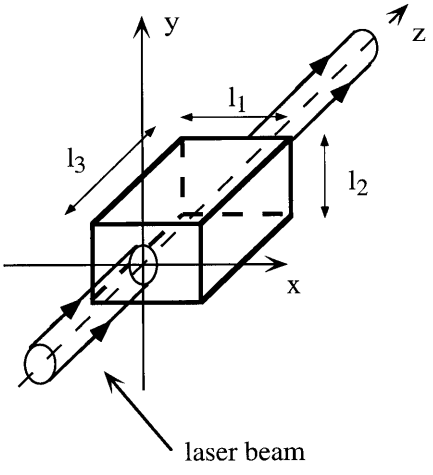

Fig. 1. Scheme of the sample defining the geometry for the calculations

where K is the thermal conductivity, $D = K/\varrho C$ is the thermal diffusivity, C is the heat capacity, ϱ the density, T the temperature rise.

Six boundary conditions are associated with (3). They take into account the heat losses through the crystal sides. These losses are assumed to be proportional to the temperature difference between the sample surfaces and their surroundings:

$$\left[\frac{\partial T(x, y, z)}{\partial x}\right]_{x=\frac{l_1}{2}} = -hT\left(\frac{l_1}{2}, y, z\right) ,$$

$$\left[\frac{\partial T(x, y, z)}{\partial x}\right]_{x=-\frac{l_1}{2}} = hT\left(-\frac{l_1}{2}, y, z\right) , \tag{4a}$$

$$\left[\frac{\partial T(x, y, z)}{\partial y}\right]_{y=\frac{l_2}{2}} = -hT\left(x, \frac{l_2}{2}, z\right) ,$$

$$\left[\frac{\partial T(x, y, z)}{\partial y}\right]_{y=-\frac{l_1}{2}} = hT\left(x, -\frac{l_2}{2}, z\right) , \tag{4b}$$

$$\left[\frac{\partial T(x, y, z)}{\partial z}\right]_{z=l_3} = -hT(x, y, l_3) ,$$

$$\left[\frac{\partial T(x, y, z)}{\partial z}\right]_{z=0} = hT(x, y, 0) , \tag{4c}$$

with $h = \frac{H}{K}$. H is the outer surface conductivity. It is usually referred to as surface conductance or the coefficient of surface heat transfer. It characterises how the sample exchanges heat energy with its surroundings.

Two configurations depicted in Fig. 2 are studied. In configuration A, the sample is suspended in air whereas in configuration B, it is sandwiched between two aluminium plates that play the role of heat sinks. In this last case,

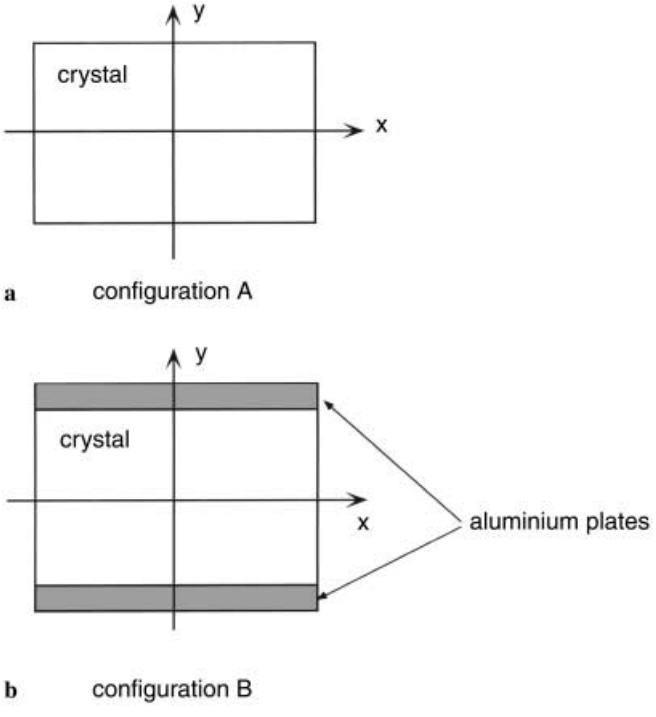

Fig. 2. Representation of the two configurations. A: crystal ideally suspended in the air, B: crystal sandwiched between two aluminium plates

the boundary conditions (4b) must be rewritten, replacing the coefficient h by h' since the outer conductivity of the crystal sides in contact with the aluminium plates is different from that of the crystal sides in contact with the air.

1.1 Steady-state solution

At stationary state, (3) simplifies as:

$$\frac{\partial^2 T(x,y,z)}{\partial x^2}+\frac{\partial^2 T(x,y,z)}{\partial y^2}+\frac{\partial^2 T(x,y,z)}{\partial z^2}=-\frac{A(x,y,z)}{K}\,, \tag{5}$$

the boundary conditions (4a–c) being unchanged.

We seek for solutions under sine and cosine series expansion and that take into account the symmetry of the problem i.e. the symmetry of the configuration associated with the symmetry of the beam. Indeed, the temperature is an even function of the variables x and y whatever the configuration (A or B). So $T(x,y,z)$ can be expanded as:

$$T(x,y,z)=\sum_{m,n,l} T_{mnl}\cos\left(\beta_m\frac{x}{l_1}\right)\cos\left(\nu_n\frac{y}{l_2}\right)\cos\left(\chi_l\frac{z}{l_3}\right) + \sum_{m,n,l} T'_{mnl}\cos\left(\beta_m\frac{x}{l_1}\right)\cos\left(\nu_n\frac{y}{l_2}\right)\sin\left(\chi_l\frac{z}{l_3}\right)\,. \tag{6}$$

In the same manner, $-\frac{A(x,y,z)}{K}$ can be expanded as:

$$-\frac{A(x,y,z)}{K}=\sum_{m,n,l}\left[C_{mnl}\cos\left(\beta_m\frac{x}{l_1}\right)\cos\left(\nu_n\frac{y}{l_2}\right)\cos\left(\chi_l\frac{z}{l_3}\right) + D_{mnl}\cos\left(\beta_m\frac{x}{l_1}\right)\cos\left(\nu_n\frac{y}{l_2}\right)\sin\left(\chi_l\frac{z}{l_3}\right)\right], \tag{7}$$

where

$$C_{mnl}=-\frac{8\alpha P}{l_1 l_2 l_3 \pi K w_0^2}\int_{-\frac{l_1}{2}}^{\frac{l_1}{2}}\int_{-\frac{l_2}{2}}^{\frac{l_2}{2}}\int_{0}^{l_3}\mathrm{e}^{-(x^2+y^2)/w_0^2} \times \mathrm{e}^{-\alpha z}\cos\left(\beta_m\frac{x}{l_1}\right)\cos\left(\nu_n\frac{y}{l_2}\right)\cos\left(\chi_l\frac{z}{l_3}\right)\mathrm{d}x\,\mathrm{d}y\,\mathrm{d}z$$

$$=-\frac{8\alpha P}{l_1 l_2 l_3 K}\,\mathrm{e}^{-\beta_m^2 w_0^2/4l_1^2}\,\mathrm{e}^{-\nu_n^2 w_0^2/4l_2^2} \times \mathrm{Re}\left[\mathrm{erf}\left(\frac{l_1}{2w_0}-\frac{\mathrm{i}\beta_m w_0}{2l_1}\right)\right]\mathrm{Re}\left[\mathrm{erf}\left(\frac{l_2}{2w_0}-\frac{\mathrm{i}\nu_n w_0}{2l_2}\right)\right]A_l\,, \tag{8}$$

with

$$A_l=-\frac{1}{\alpha^2+\chi_l^2/l_3^2}\left[\alpha\left(\mathrm{e}^{-\alpha l_3}\cos\chi_l-1\right)-\frac{\chi_l}{l_3}\mathrm{e}^{-\alpha l_3}\sin\chi_l\right]$$

and

$$D_{mnl}=-\frac{8\alpha P}{l_1 l_2 l_3 \pi K w_0^2}\int_{-\frac{l_1}{2}}^{\frac{l_1}{2}}\int_{-\frac{l_2}{2}}^{\frac{l_2}{2}}\int_{0}^{l_3}\mathrm{e}^{-(x^2+y^2)/w_0^2} \times \mathrm{e}^{-\alpha z}\cos\left(\beta_m\frac{x}{l_1}\right)\cos\left(\nu_n\frac{y}{l_2}\right)\sin\left(\chi_l\frac{z}{l_3}\right)\mathrm{d}x\,\mathrm{d}y\,\mathrm{d}z$$

$$=-\frac{8\alpha P}{l_1 l_2 l_3 K}\,\mathrm{e}^{-\beta_m^2 w_0^2/4l_1^2}\,\mathrm{e}^{-\nu_n^2 w_0^2/4l_2^2} \times \mathrm{Re}\left[\mathrm{erf}\left(\frac{l_1}{2w_0}-\frac{\mathrm{i}\beta_m w_0}{2l_1}\right)\right]\mathrm{Re}\left[\mathrm{erf}\left(\frac{l_2}{2w_0}-\frac{\mathrm{i}\nu_n w_0}{2l_2}\right)\right]B_l\,, \tag{9}$$

with

$$B_l=-\frac{1}{\alpha^2+\chi_l^2/l_3^2}\left[\alpha\,\mathrm{e}^{-\alpha l_3}\sin\chi_l+\frac{\chi_l}{l_3}\left(\mathrm{e}^{-\alpha l_3}\cos\chi_l-1\right)\right]\,.$$

In these expressions, erf designates the error function [17]. Reporting (6) in (5) and identifying the terms in sine and cosine, respectively, we get :

$$T_{mnl}=-\frac{C_{mnl}}{\left(\frac{\beta_m}{l_1}\right)^2+\left(\frac{\nu_n}{l_2}\right)^2+\left(\frac{\chi_l}{l_3}\right)^2}\,, \tag{10}$$

$$T'_{mnl}=-\frac{D_{mnl}}{\left(\frac{\beta_m}{l_1}\right)^2+\left(\frac{\nu_n}{l_2}\right)^2+\left(\frac{\chi_l}{l_3}\right)^2}\,. \tag{11}$$

The boundary conditions (4a–c) lead with (6) to the transcendental equations whose roots are the quantities β_m, ν_n, χ_l:

$$\frac{\beta_m}{2}\tan\frac{\beta_m}{2}=\frac{hl_1}{2}\,, \tag{12a}$$

$$\frac{\nu_n}{2}\tan\frac{\nu_n}{2}=\frac{hl_2}{2}\,, \tag{12b}$$

$$\tan\chi_l=\frac{2\chi_l h l_3}{\chi_l^2-h^2 l_3^2}\,. \tag{12c}$$

With the numerical values of the parameters $h=4\,\mathrm{m}^{-1}$, $l_1=5\,\mathrm{mm}=l_2=l_3$ or with the values of our samples, the quantities hl_1, hl_2, hl_3 are lower than 1 so that the roots of the above equations can be well approximated as (the agreement is better than 97%):

$$\beta_1=\sqrt{2hl_1},\quad \beta_m=2m\pi+\frac{hl_1}{m\pi}\quad \text{for } m>1\,, \tag{13a}$$

$$\nu_1=\sqrt{2hl_2},\quad \nu_n=2n\pi+\frac{hl_2}{n\pi}\quad \text{for } n>1\,, \tag{13b}$$

$$\chi_1=\sqrt{2hl_3},\quad \chi_l=l\pi+\frac{2hl_3}{l\pi}\quad \text{for } l>1\,. \tag{13c}$$

Let us calculate the temperature rise at two particular points of the crystal. At the center of the input face, it is equal to:

$$T(0,0,0)=\sum_{m,n,l}T_{mnl}=\sum_{m,n,l}-\frac{C_{mnl}}{\left(\frac{\beta_m}{l_1}\right)^2+\left(\frac{\nu_n}{l_2}\right)^2+\left(\frac{\chi_l}{l_3}\right)^2}\,. \tag{14}$$

For values of the parameters, $l_1=5\,\mathrm{mm}=l_2=l_3$, $h=4\,\mathrm{mm}^{-1}$, $\alpha=1\,\mathrm{cm}^{-1}$, $P=1\,\mathrm{W}$, $w_0=12\,\mu\mathrm{m}$ and $K=5.5\,\mathrm{W\,K^{-1}m^{-1}}$ [18], the summation can be bounded to the first term T_{111} because all the others are 330 times lower if the waist value is greater than 10 μm, the other parameters being unchanged. So that

$$T(0,0,0)\approx-\frac{C_{111}}{\left(\frac{\beta_1}{l_1}\right)^2+\left(\frac{\nu_1}{l_2}\right)^2+\left(\frac{\chi_1}{l_3}\right)^2}\,, \tag{15}$$

or, more explicitly, since the real part of the error function is close to unity:

$$T(0,0,0)\approx\frac{4P(1-\mathrm{e}^{-\alpha l_3})}{H(l_1l_2+l_1l_3+l_2l_3)}\approx\frac{4P\alpha l_3}{H(l_1l_2+l_1l_3+l_2l_3)}\,. \tag{16}$$

At the corner of the input face of the sample, the temperature rise is:

$$\begin{aligned}T\left(\frac{l_1}{2},\frac{l_2}{2},0\right)&=\sum_{m,n,l}T_{mnl}\cos\left(\frac{\beta_m}{2}\right)\cos\left(\frac{\nu_n}{2}\right)\\&\approx T_{111}\cos\left(\frac{\beta_1}{2}\right)\cos\left(\frac{\nu_1}{2}\right)\\&=T(0,0,0)\cos\left(\frac{\beta_1}{2}\right)\cos\left(\frac{\nu_1}{2}\right)\,.\end{aligned} \tag{17}$$

This gives the ratio between the temperature rise at the corner and at the center of the entrance face:

$$\frac{T\left(\frac{l_1}{2},\frac{l_2}{2},0\right)}{T(0,0,0)}=\cos\left(\frac{\beta_1}{2}\right)\cos\left(\frac{\nu_1}{2}\right)\,. \tag{18}$$

1.2 Kinetics of the temperature rise

In this case, a solution of the three-dimensional time-dependent heat equation (3) has to be found. Using a similar formalism as that proposed in the preceding subsection, assuming that at the initial time the crystal is at room temperature, $T(x,y,z)$ is expanded according to (19):

$$\begin{aligned}T(x,y,z,t)=\sum_{m,n,l}\Bigg[&T_{mnl}\cos\left(\beta_m\frac{x}{l_1}\right)\cos\left(\nu_n\frac{y}{l_2}\right)\cos\left(\chi_l\frac{z}{l_3}\right)\\&+T'_{mnl}\cos\left(\beta_m\frac{x}{l_1}\right)\cos\left(\nu_n\frac{y}{l_2}\right)\sin\left(\chi_l\frac{z}{l_3}\right)\Bigg]\\&\times\left[1-\mathrm{e}^{-t/\tau_{mnl}}\right]\,.\end{aligned} \tag{19}$$

The expression for $-\frac{A(x,y,z)}{K}$ is maintained. Reporting (19) in (3) and identifying the terms in sine and cosine, respectively, we get:

$$\tau_{mnl}=\frac{1}{D}\times\frac{1}{\left(\frac{\beta_m}{l_1}\right)^2+\left(\frac{\nu_n}{l_2}\right)^2+\left(\frac{\chi_l}{l_3}\right)^2}\,. \tag{20}$$

With the values $l_1=5\,\mathrm{mm}=l_2=l_3$, $h=4\,\mathrm{m}^{-1}$, $\alpha=1\,\mathrm{cm}^{-1}$, $P=1\,\mathrm{W}$, $w_0=12\,\mu\mathrm{m}$ and for the case of undoped barium titanate $K=5.5\,\mathrm{W\,K^{-1}m^{-1}}$, $\varrho=6020\,\mathrm{kg\,m^{-3}}$, $C=430\,\mathrm{J\,kg^{-1}K^{-1}}$ [19], it is found that the time constant τ_{111} given by

$$\tau_{111}=\frac{\varrho C}{2H}\frac{l_1l_2l_2}{l_1l_2+l_2l_3+l_1l_3} \tag{21}$$

is 80 times larger than all the other time constants. Moreover, the numerical calculations reveal that the first term ($m=1$, $n=1$, $l=1$) of the summation in the first bracket in (19) is at least 10 times greater than all the other terms whatever are the coordinates (x,y,z) of a point in the crystal. Consequently, it can be concluded that the kinetics of the temperature rise can be well approximated with a mono-exponential law.

2 Experimental results

This section is devoted to the experimental part of the work. First, the experimental arrangement is described. Its interest lies in the fact that it includes the laser source that illuminates the crystal and the optical setup to observe, detect and record in real time the appearance or the evolution of the defects in the sample. The second subsection presents the results obtained under cw illumination with an argon laser. The interests of the cw study are to connect the results with the calculations developed in Sect. 1, to deduce the outer conductivity of the crystal faces and to analyse the behaviour of the materials under intense cw laser irradiation. The last subsection is dedicated to the more agressive and destructive regime that is the pulsed nanosecond illumination with a Nd:YAG laser. The damage threshold of a $BaTiO_3$ crystal is measured and defects are detected within the volume of another $BaTiO_3$ crystal.

2.1 Experimental setup

Our experimental arrangement is made up of many blocks as drawn in Fig. 3. In the block I, the beam issued from an argon laser operating at $\lambda=514.5\,\mathrm{nm}$ is focused in the middle of the crystal with a microscope objective. The half-wave plate HW1 and the polarizer P adjust the direction of the light polarization. The three other blocks (II-IV) are designed to detect and follow the evolution of the defects and strains that arise within the crystal. For this, a He-Ne laser ($\lambda=632.8\,\mathrm{nm}$) is used. It delivers a low power so that its influence on the thermal effects induced in the crystal can be neglected. It is expanded and well collimated after passing through a spatial filter. Its polarization direction is adjusted with the half-wave HW2. The cube beam splitter CBS transmits a part of the He-Ne laser that is then reflected on the front and rear faces of the

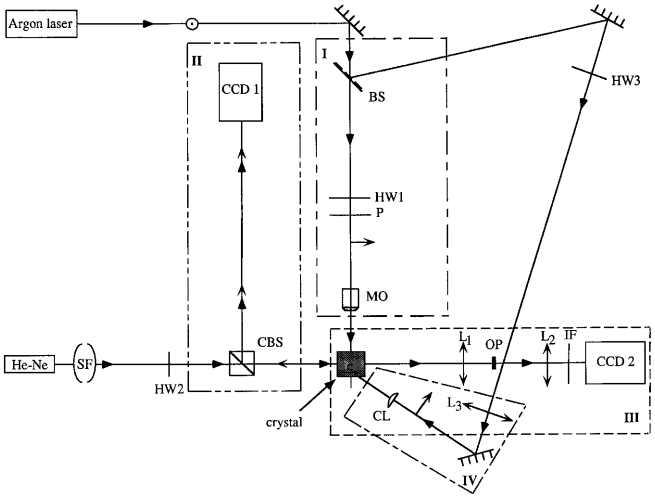

Fig. 3. Experimental arrangement for the irradiation of the crystal (block I), the observation of the defects (blocks III-IV) and the strains (block II). HW1, HW2, HW3, half-wave plates; P, polarizer; CBS, cube beam splitter; BS, beam splitter; SF, spatial filter; L_1, L_2, L_3, lenses; OP, opaque object; IF, bandpass interference filter; MO, microscope objective

crystal so that interferences occur. The interference pattern is imaged on a CCD camera (CCD1). This block II allows us in particular to visualize the strains inside the sample.

A part of the incident He-Ne beam is transmitted through the crystal. The detection of diffusive defects in its volume is led with a classical strioscopy arrangement also called central dark ground method of observation [20] (block III). OP is an opaque object that stops the directly transmitted rays so only the rays deviating by the diffusive defects are imaged on the CCD camera (CCD2). A bandpass interference filter (IF) centered at $\lambda = 632.8$ nm and whose bandwith is $\Delta\lambda = 10$ nm is put in front of the camera to stop the light of the argon laser that may be diffused in the direction of CCD2. The block IV is built by deviating a small amount of the argon laser light with beam splitter BS. The beam is then focused in the crystal with a cylindrical lens CL. As more completely described in [21], this arrangement detects the antiparallel ferroelectric domains that could appear. These domains are imaged on CCD2. In this case, IF is replaced by another bandpass interference filter centered at $\lambda = 514.5$ nm.

A thin chromel–alumel thermocouple wire 350 μm in diameter is glued with silver paste on one corner ($x = l_1/2$, $y = l_2/2$, $z = 0$) of the entrance face (relative to the argon laser beam) of the crystal. The cold junction is maintained at a constant temperature by putting it in a massive piece of aluminium. The recording of the temperature is performed using a Keithley 195A digital multimeter. The accuracy of the temperature measurement is ± 0.2 °C.

To close this subsection, it must be emphasized that the experimental setup can be used for a variety of crystals for which the problem of damage threshold arises: we can list crystals that possess photorefractive sensitivity such as $BaTiO_3$, $KNbO_3$, $Bi_{12}SiO_{20}$, $Bi_{12}TiO_{20}$, $LiNbO_3$, $LiIO_3$, crystals inserted in devices for frequency doubling the laser light from laser diodes ($KNbO_3$), materials involved in harmonic generation: KH_2PO_4, BaB_2O_4, LiB_3O_5, $LiNbO_3$.

2.2 Continuous-wave illumination

2.2.1 Comparison between configuration A and configuration B. The comparison of the two configurations (Fig. 2) is conducted with two barium titanate crystals grown at FEE by the top seeded solution growth method. One of them, called S_1 is a nominally undoped crystal with dimensions $l_1 \times l_2 \times l_3 = a_1 \times a_2 \times c = 5.9 \times 5.1 \times 4.2$ mm. The other crystal (S_2) is a cobalt–rhodium-doped crystal (20 ppm of Co and 10^3 ppm of Rh in the melt) with dimensions $l_1 \times l_2 \times l_3 = a_1 \times a_2 \times c = 4.5 \times 4.6 \times 5.2$ mm. These samples are 0° oriented; all their faces are optically polished. Some defects such as growth zones are present inside these crystals.

The argon beam is focused inside the crystal, the corresponding intensity is 25.7 kW/mm^2. The temporal variations of the temperature taken at the corner ($x = l_1/2$, $y = l_2/2$, $z = 0$) are plotted in Fig. 4 for sample S_2 for the two configurations A and B. Numerical adjustments of these curves with mono-exponential laws give reasonably good results so that the time constants can be deduced: $\tau = (17 \pm 1)$ s for configuration A, $\tau = (58 \pm 2)$ s for configuration B. This is in agreement with the theoretical development of Sect. 1 that showed that one time constant (τ_{111}) is predominant and so the kinetic curve can be considered as mono-exponential.

The steady-state temperature reached with configuration B is lower than that with configuration A. This illustrates the role of the two aluminium plates in configuration B which act like cold sources and help the evacuation of the heat. Nevertheless, with this last configuration, there are some regions within the crystal where the resulting strains will be greater than those in configuration A since the temperature gradient is more important in configuration B. This is well illustrated by the thermal images (Fig. 5a,b) showing the longitudinal temperature distribution inside sample S_2. Similar results are obtained with sample S_1. In particular, for configuration A the time constant is $\tau = (22 \pm 1)$ s and for configuration B it is $\tau = (62 \pm 2)$ s. From the thermal images, the steady-state temperatures at two particular points are $T(0, 0, 0) = 32.4$ °C and $T(l_1/2, l_2/2, 0) = 28.2$ °C. From this, the ratio between the temperature rise at the corner of the crystal and at the centre of the entrance face is deduced to be 0.87. With this value

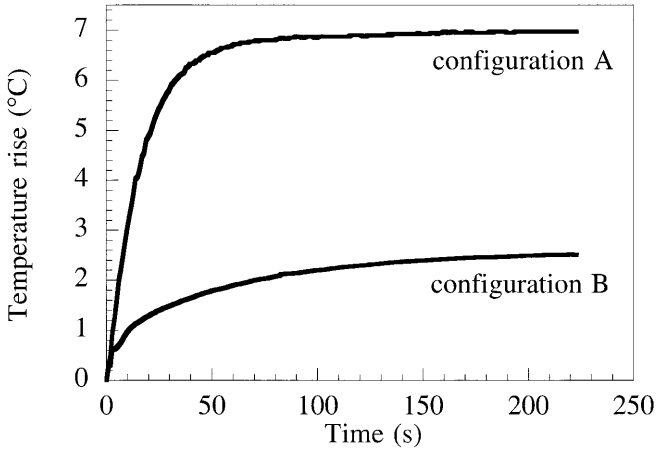

Fig. 4. Experimental kinetics curves of the temperature rise for sample S_2. The intensity of the argon laser is 25.7 kW/mm^2

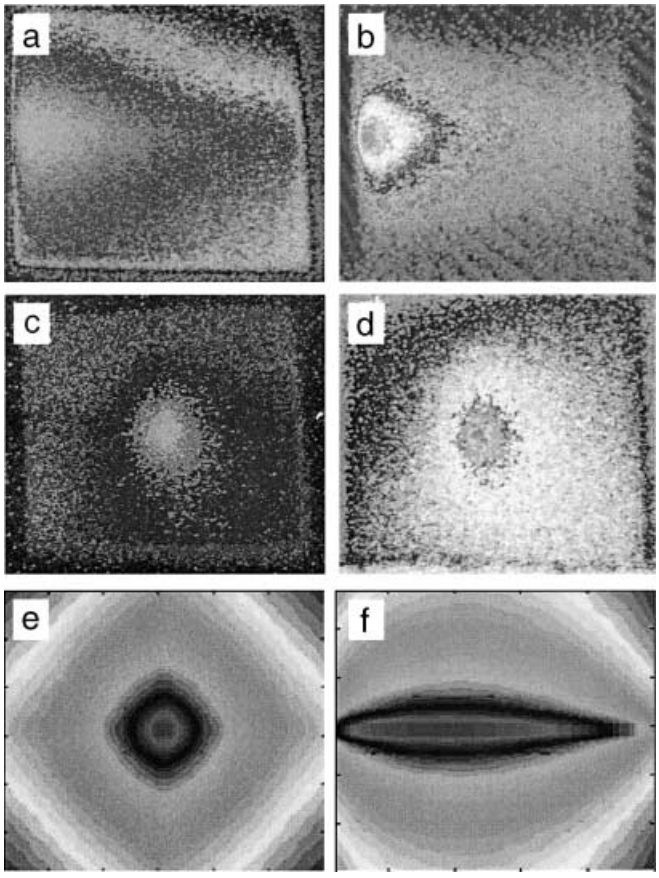

Fig. 5a–f. Maps of the temperature repartition for sample S_2. **a** Longitudinal temperature repartition for the crystal mounted according to configuration A. **b** Longitudinal temperature repartition for the crystal mounted according to configuration B. **c** Temperature repartition at the input face for the crystal mounted according to configuration A. **d** Temperature repartition at the input face for the crystal mounted according to configuration B. **e**, **f** Calculated temperature distributions in configuration A

Table 1. Thermal conductivities, heat capacities, temperature elevations and time constants for extraordinarily polarized (extr. pol.) and ordinarily polarized (ord. pol.) light. The configuration B is used

		$BaTiO_3$ (S_1)	$BaTiO_3$:Rh,Co (S_2)
K ($W K^{-1} m^{-1}$)	at 300 K	3.6 ± 0.3	2.1 ± 0.2
C ($J kg^{-1} K^{-1}$)	at 300 K	435 ± 5	435 ± 5
Temperature rise ΔT^{ss}	extr. pol.	1.5	1.9
at steady state (°C)	ord. pol.	1.8	2.2
$\frac{\Delta T^{ss,ordi}}{\Delta T^{ss,extra}}$		1.2 ± 0.3	1.2 ± 0.2
$\frac{A^{ordi}}{A^{extra}}$		1.25 ± 0.20	1.18 ± 0.13
Time constant τ(s)	extr. pol.	64 ± 2	59 ± 2
	ord. pol.	64 ± 2	60 ± 2

and (18), the outer conductivities of the samples in configuration A are found to be $H_{S_2} = 122\,W K^{-1} m^{-2}$ for sample S_2 and $H_{S1} = 100\,W K^{-1} m^{-2}$ for sample S_1. Then, the time constants given by (21) are $\tau = 17$ s for sample S_1 and $\tau = 22$ s for sample S_2 in good agreement with the experimental values given above.

It is observed experimentally that the time constants are independent of the intensity. This is in accordance with the theoretical expression given by (20). We have also checked that the steady state temperature grows linearly the incident power, as predicted by (10) and (11) for which the coefficients T_{mnl} and T'_{mnl} are directly proportional to the power P.

The results presented in this part validate the theoretical development on the dynamics and the steady-state temperature distribution.

2.2.2 Influence of the nature of the doping. In this paragraph, the incident intensity is fixed at $20.2\,kW/mm^2$, the beam is extraordinarily polarized. The crystals S_1 and S_2 are sandwiched between two aluminium plates (configuration B). For each of them, the temporal rise of temperature is monitored. From the data, the time constants for S_1 and S_2 are found to be respectively $\tau_{S1} = (68 \pm 2)$ s, $\tau_{S2} = (62 \pm 2)$ s and the temperature rise at steady state are $\Delta T^{ss}_{S_1} = (1.4 \pm 0.2)$ °C and $\Delta T^{ss}_{S_2} = (2.1 \pm 0.2)$ °C. The difference between these two last values is a direct consequence of the absorption coefficient α. In fact, the absorbed power A is:

$$A = (1 - R)(1 - e^{-\alpha l_3}) , \tag{22}$$

where R is the reflexion coefficient under normal incidence at the interface air/crystal. The absorption coefficients measured at $\lambda = 514.5$ nm for extraordinarily polarized light are $\alpha^e_{S_1} = 0.6\,cm^{-1}$ and $\alpha^e_{S_2} = 1.8\,cm^{-1}$. From this, the ratio of the steady-state temperatures $\frac{\Delta T^{ss}_{S_1}}{\Delta T^{ss}_{S_2}} = 0.6 \pm 0.2$ can be compared to that of the absorbed powers $\frac{A_{S_1}}{A_{S_2}} = 0.54 \pm 0.08$ and found to be very close to each other and in accordance with their relative uncertainties. So, the different values of the steady-state temperatures mainly come from the absorption coefficients. The dependence of the thermal conductivity on the nature of the doping (see Table 1) may explain the different time constants τ_{S_1} and τ_{S_2}.

2.2.3 Influence of the light polarization. At a given input intensity of $25.7\,kW/mm^2$, the time constants and the steady-state temperature elevations are deduced from the kinetics curves in a similar way to that described in the above paragraph. The configuration B is used. The results are gathered in Table 1. Once again, the difference between the steady-state temperatures is satisfactorily explained by taking into account the absorption coefficients of the crystals (22).

2.2.4 Defects induced by the laser radiation. Four barium titanate crystals are put at our disposal to lead this study. Each of them have been grown at FEE by the top seeded solution growth method. Sample S_3 is a cobalt–rhodium-doped crystal (20 ppm of Co and 10^3 ppm of Rh in the melt) with dimensions $l_1 \times l_2 \times l_3 = a_1 \times a_2 \times c = 5.5 \times 3.1 \times 5.3$ mm, samples S_4 and S_5 are nominally undoped crystals with the respective dimensions of $l_1 \times l_2 \times l_3 = a_1 \times a_2 \times c = 3.2 \times 2.6 \times 5.1$ mm and $l_1 \times l_2 \times l_3 = a_1 \times a_2 \times c = 5.3 \times 1.9 \times 5.9$ mm, the crystal S_6 is a cobalt-doped crystal (20 ppm of Co in the melt) with dimensions $l_1 \times l_2 \times l_3 = a_1 \times a_2 \times c = 3 \times 3 \times 1$ mm. These samples are 0° oriented; all their faces are optically polished.

The intensity of the laser is $25.7\,kW/mm^2$, each crystal is irradiated during 13–14 h. The extraordinarily polarized light

Table 2. Evolution, detection and location of the defects in four barium titanate crystals irradiated with a cw argon laser operating at 514.5 nm. The intensity in the crystal is 25.7 kW/mm^2

Crystal	$BaTiO_3$:Rh,Co (S_3)	$BaTiO_3$ (S_4)	$BaTiO_3$ (S_5)	$BaTiO_3$:Co (S_6)
Optical quality before irradiation	Few diffusive defects within the volume Very few surface defects Typical input face RMS: 0.75 nm	Few diffusive defects within the volume Very few surface defects Typical input face RMS: 0.99 nm	Diffusive defects within the volume. Very few surface defects Typical input face RMS: 1.01 nm	Diffusive defects within the volume. Typical input face RMS: 95 nm (faces unpolished)
Duration of cw illumination	13 h	13 h	14 h	13 h
Strioscopy observation during and after irradiation	No evolution of the diffusive defects.	No evolution of the diffusive defects.	No evolution of the diffusive defects.	No evolution of the diffusive defects.
Comparison of the interference patterns before, during and after the irradiation	No fringe distortion, fringe shift during the illumination.	No fringe distortion, fringe shift during the illumination.	No fringe distortion, fringe shift during the illumination.	No fringe distortion, fringe shift during the illumination.
Antiparallel ferroelectric domains	No domain within the volume.	No domain within the volume.	No domain within the volume.	No domain within the volume.
Surface defects after irradiation	No surface defects	Defects on the input and output faces Input face RMS: 2.47 nm Output face RMS: 1.80 nm	Defects on the input face (RMS = 2.57 nm)	No surface defects

of the argon laser is incident at the input face that contains the *c*-axis; this configuration is in accordance with the practical arrangements that use $BaTiO_3$ crystals [22] (the highest performances in wave-mixing are obtained in such an orientation). The defects are continuously detected with blocks II-IV of the experimental setup. The results are listed in Table 2. The root-mean-square (RMS) values are calculated from data acquisition performed with an optical profilometer (EOTECH Micromap 512/550).

In a general way, no defect appears within the crystals after the irradiation. If defects appear, they are located at the input face (Fig. 6b) and a few defects are at the exit face (Fig. 6c). This corroborates the thermal images in Fig. 5a,b revealing that the thermal rise is the highest at the input face and its neighbouring. This is also in accordance with the theoretical and experimental works already done on the subject [23, 24]. An interesting feature is that the strains induced by the argon laser are completely reversible since with the block II of the experimental setup, identical interference patterns are observed before the irradiation and then after the argon laser is cut off and once the crystal temperature goes down the ambient temperature (Fig. 7). This tends to prove that the deformation is reversible.

2.3 Pulsed regime

The laser is a frequency-doubled Q-switched Nd:YAG operating at $\lambda = 532$ nm, providing a TEM_{00} mode and delivering pulses of 5 ns at a repetition rate of 25 Hz. The experiments are conducted on two barium titanate crystals. One of them, called S_7, is a cobalt–rhodium-doped crystal (20 ppm of Co and 10^3 ppm of Rh in the melt) with dimensions $l_1 \times l_2 \times l_3 = a_1 \times a_2 \times c = 2.3 \times 4.6 \times 4.1$ mm. The other sample, called S_8, is a nominally undoped crystal with the dimensions of $l_1 \times l_2 \times l_3 = a_1 \times a_2 \times c = 3.2 \times 2.6 \times 5.1$ mm. These samples are 0° oriented; all their faces are optically polished.

Because of the high-power pulses, the beam is not focused inside the crystal, it converges with a lens ($f = 120$ mm) put

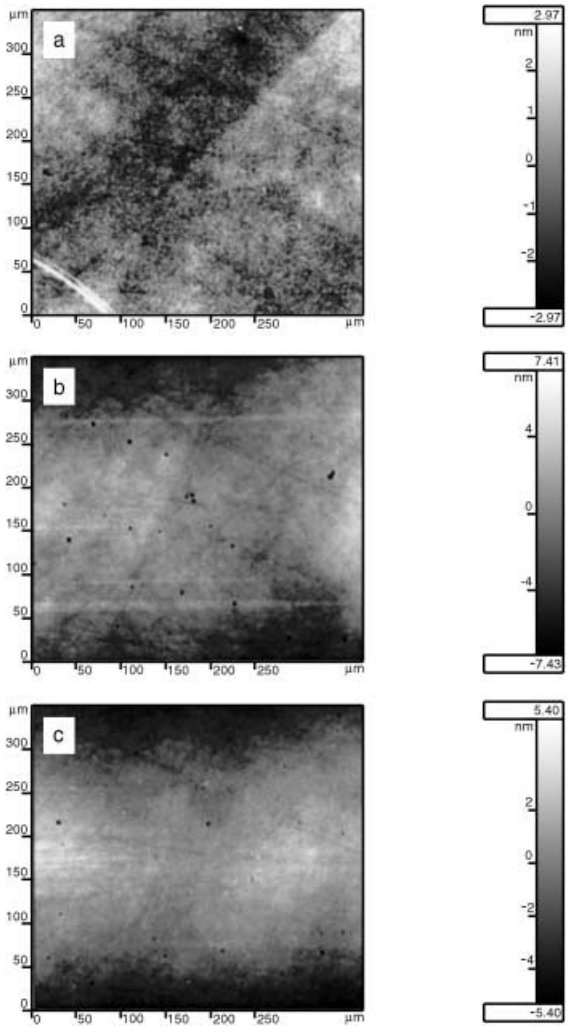

Fig. 6a–c. Typical aspects of the input and output faces for sample S_4. **a** Input face before the irradiation. **b** Input face after laser irradiation at 514.5 nm with an intensity of 25.7 kW/mm^2 during 13 h. **c** Output face after the irradiation. The images **a** and **b** are taken at the laser spot impact on the input face. Image **c** is taken at the output face of the crystal

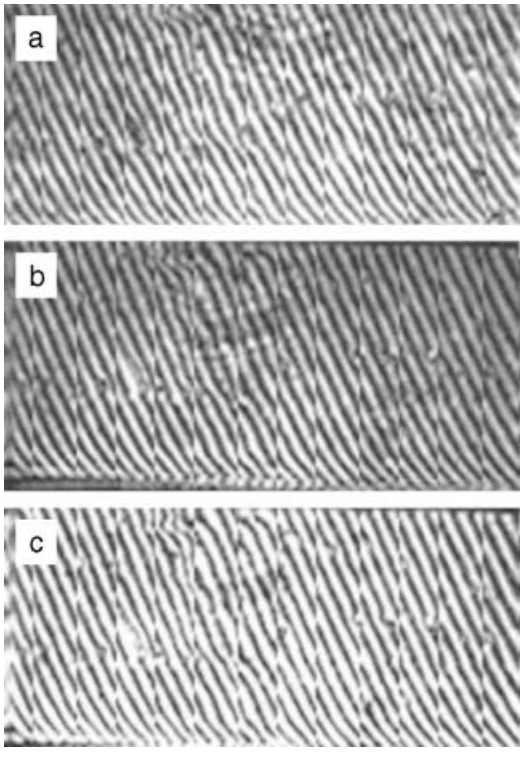

Fig. 7a–c. Interference patterns recorded with block II for sample S_5. **a** Before the irradiation. **b** After 13 h of laser irradiation at 514.5 nm with an intensity of 25.7 kW/mm^2, the image is taken just before the laser beam is cut off.**c** Image taken once the crystal temperature recovers the ambient value

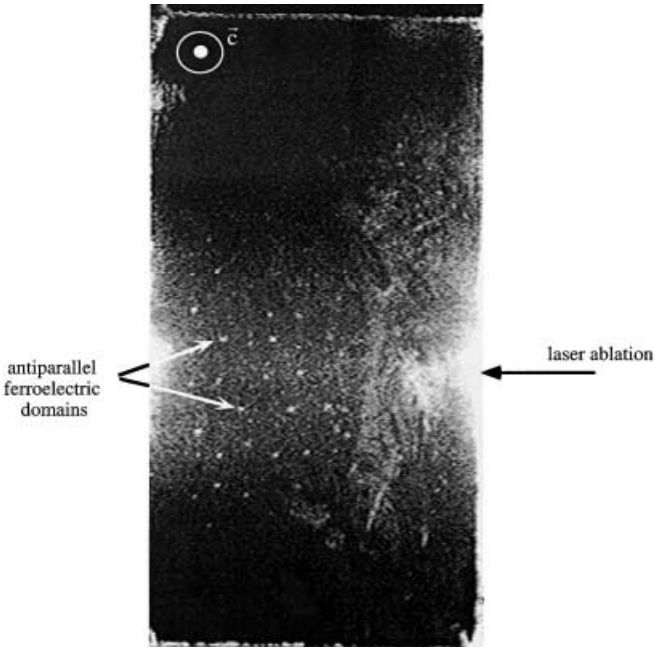

Fig. 8. Antiparallel ferroelectric domains created with the pulsed Nd:YAG laser within sample S_8. The *black arrow* indicates the location of the laser ablation. The bright spots correspond to domains whose *c*-axis is reversed

at a distance of 6 cm from the entrance face of the crystal. The beam polarization is extraordinary for the same reasons as those invoked in Sect. 2.2.4.

After illuminating the $BaTiO_3$:Rh,Co sample during one hour with pulses whose peak power is $P_C = 4.2$ MW, no evolution inside the crystal and at its surfaces is noted. Then, after two hours of laser irradiation at $P_C = 9.2$ MW, small defects localized on the input face and at the vicinity of the beam are observed. They are similar to the defects shown in Fig. 6c. No defect appears inside the volume of the crystal. The damage threshold is reached after 3 s of illumination and is 0.44 GW/cm^2. Once the damage is reached, small defects arise on the input face. Their size and quantity are more important in comparison with those present before the damage threshold test.

The sample S_8 is illuminated during one hour with peak power pulses of $P_C = 4.2$ MW. This results in the appearance of some domains at the input face. Then, during one hour, the peak power being $P_C = 9.2$ MW, this induces an ablation of the input face. Nevertheless, it must be noted that the interference patterns before and after the ablation are the same. So, once again, no permanent strains are induced inside the crystal. The damage threshold is reached after 6 s of illumination and is 0.54 GW/cm^2 in accordance with the value mentioned in [25]. Once it is reached, antiparallel ferroelectric domains are detected with block IV inside the crystal volume (Fig. 8). The principle of this method is more detailed in our previous study [21]. The bright spots correspond to zones where the *c*-axis is reversed and reveal the polydomain character of the sample.

3 Conclusion

The thermal gradient in a crystal irradiated by a Gaussian distribution of light is calculated taking into account the finite size of the sample in each direction and the heat losses through its sides. The theoretical solution for the kinetics of the temperature rise reveals that the phenomenon can be considered as mono-exponential. For the steady-state and the dynamics regime, the solutions of the heat equation are found under sine and cosine series. The experiments conducted under the cw illumination of an argon laser validate the theoretical analysis. If the crystal is sandwiched between two aluminium plates the thermal gradient being high in some regions of the crystal, the induced strains are non-negligible and can result in an index change that may be of importance in non-linear crystals used in harmonic generation for which the phase-matching condition is a critical parameter. Irradiating various barium titanate crystals with a cw laser illumination, no new defect such as diffusive centres or antiparallel ferroelectric domains has appeared within their volume. Only defects at the input surface are generated and a few at the output face. It can be concluded that in practical devices using the photorefractive properties of barium titanate such defects are not a penalty since the holographic grating is recorded inside the crystal. Under pulsed regime, the laser ablation of the input face is observed as well as the creation of antiparallel ferroelectric domains within the crystal. Efforts are necessary to better understand this more destructive regime: a theoretical analysis of the dynamics that takes into account the temporal shape of the pulses is needed. A temporal recording of the thermal gradient build-up should be useful. The design of resistant optical coatings could be a solution to avoid the surface damage.

Acknowledgements. The authors are pleased to acknowledge Nathalie Roudergues and Daniel Stuerga of the Laboratoire de Recherches sur la Réactivité des Solides (Université de Bourgogne, Dijon, France) for providing the thermal camera and for their assistance on its working. We also gratefully thank Mario Maglione for his helpful advices about the continuous recording of the temperature with a Keithley digital multimeter. The measurements under pulsed regime could not have been conducted without the help of Guy Millot who offered to put at our disposal his Nd:YAG pulsed laser.

References

1. W. Koechner: Appl. Opt. **9**, 1429 (1970)
2. E.P. Riedel, G.D. Baldwin: J. Appl. Phys. **38**, 2720 (1967)
3. G.D. Baldwin, E.P. Riedel: J. Appl. Phys. **38**, 2726 (1967)
4. F.W. Quelle, Jr: Appl. Opt. **5**, 633 (1966)
5. B.W. Woods, S.A. Payne, J.E. Marion, R.S. Hughes, L.E. Davis: J. Opt. Soc. Am. B **8**, 970 (1991)
6. L. Holtmann: Phys. Status Solidi A **113**, K89 (1989)
7. G.A. Brost, R.A. Motes, J.R. Rotge: J. Opt. Soc. Am. B **5**, 1879 (1988)
8. P. Mathey, P. Jullien, B. Mazué, D. Rytz: J. Opt. Soc. Am. B **15**, 1353 (1998)
9. S. Campbell, S.-H. Lin, X. Yi, P. Yeh: J. Opt. Soc. Am. B **13**, 2218 (1996)
10. K. Buse, K.H. Ringhofer: Appl. Phys. A **57**, 161 (1993)
11. K. Buse, R. Pankrath, E. Krätzig: Opt. Lett. **19**, 260 (1994)
12. D. Kip, E. Krätzig, V. Shandarov, P. Moretti: Opt. Lett. **23**, 343 (1998)
13. A. Dazzi, P. Mathey, P. Lompré, P. Jullien, S.G. Odoulov, P. Moretti: J. Opt. Soc. Am. B **16**, 256 (1999)
14. F.A. MacDonald: Appl. Phys. Lett. **54**, 1504 (1989)
15. Y. Lu, S. Zhang, J. Cheng: Appl. Phys. B **70**, 85 (2000)
16. H.S. Carslaw, J.C. Jaeger: *Conduction of Heat in Solids*, 2nd edn. (Clarendon Press, Oxford 1959)
17. M. Abramowitz, I.A. Stegun: *Handbook of Mathematics Functions* (NBS, Washington 1964)
18. A.J.H. Mante, J. Volger: Phys. Lett. **24A**, 139 (1967)
19. I. Hatta, A. Ikushima: J. Phys. Soc. Jap. **41**, 558 (1976)
20. M. Born, E. Wolf: *Principles of Optics*, 6th edn. (Pergamon Press, Oxford 1993)
21. P. Mathey, P. Jullien, P. Lompré, D. Rytz: Appl. Phys. A **66**, 511 (1998)
22. Y. Fainman, E. Klancnik, S.H. Lee: Opt. Eng. **25**, 228 (1986)
23. N.L. Boling, M.D. Crisp, G. Dubé: Appl. Opt. **12**, 650 (1973)
24. N. Bloembergen: Appl. Opt. **12**, 661 (1973)
25. D. Mahgerefth: PhD Thesis, Univ. of Southern California (1990) p. 20